

Lawrence Berkeley National Laboratory

LBL Publications

Title

Electric-field-tuned topological phase transition in ultrathin Na₃Bi

Permalink

<https://escholarship.org/uc/item/5sw3q991>

Journal

Nature, 564(7736)

ISSN

0028-0836

Authors

Collins, James L

Tadich, Anton

Wu, Weikang

et al.

Publication Date

2018-12-01

DOI

10.1038/s41586-018-0788-5

Peer reviewed

Electric Field-Tuned Topological Phase Transition in Ultra-Thin Na₃Bi

James L. Collins^{1,2,3}, Anton Tadich^{3,4}, Weikang Wu⁵, Lidia C. Gomes^{6,7}, Joao N. B. Rodrigues^{6,8}, Chang Liu^{1,2,3}, Jack Hellerstedt^{1,2}, Hyejin Ryu^{9,10}, Shujie Tang⁹, Sung-Kwan Mo⁹, Shaffique Adam^{6,11}, Shengyuan A. Yang^{5,12}, Michael S. Fuhrer^{1,2,3}, Mark T. Edmonds^{1,2,3*}

1. School of Physics and Astronomy, Monash University, Clayton VIC 3800, Australia
2. Monash Centre for Atomically Thin Materials, Monash University, Clayton VIC 3800 Australia
3. Centre for Future Low Energy Electronics Technologies, Monash University, Clayton VIC 3800 Australia
4. Australian Synchrotron, 800 Blackburn Road, Clayton, VIC 3168, Australia
5. Research Laboratory for Quantum Materials & EPD Pillar, Singapore University of Technology and Design, Singapore 487372, Singapore
6. Department of Physics and Centre for Advanced 2D Materials, National University of Singapore, 117551, Singapore
7. National Centre for Supercomputing Applications, University of Illinois at Urbana-Champaign, Champaign, IL 61820, USA
8. Institute for Condensed Matter Theory and Department of Physics, University of Illinois at Urbana-Champaign, Champaign, IL 61820, USA
9. Advanced Light Source, Lawrence Berkeley National Laboratory, Berkeley, CA 94720, USA
10. Centre for Spintronics, Korea Institute of Science and Technology, Seoul 02792, Korea
11. Yale-NUS College, 6 College Avenue East, 138614, Singapore
12. Centre for Quantum Transport and Thermal Energy Science, School of Physics and Technology, Nanjing Normal University, Nanjing 210023, China

* Corresponding author - mark.edmonds@monash.edu

Abstract –

The electric field induced quantum phase transition from topological to conventional insulator has been proposed as the basis of a topological field effect transistor [1-4]. In this scheme an electric field can switch ‘on’ the ballistic flow of charge and spin along dissipationless edges of the two-dimensional (2D) quantum spin Hall insulator [5-9], and when ‘off’ is a conventional insulator with no conductive channels. Such a topological transistor is promising for low-energy logic circuits [4], which would necessitate electric field-switched materials with conventional and topological bandgaps much greater than room temperature, significantly greater than proposed to date [6-8]. Topological Dirac semimetals (TDS) are promising systems in which to look for topological field-effect switching, as they lie at the boundary between conventional and topological phases [3,10-16]. Here we use scanning probe microscopy/spectroscopy (STM/STS) and angle-resolved photoelectron spectroscopy (ARPES) to show that mono- and bilayer films of TDS Na₃Bi [3,17] are 2D topological insulators with bulk bandgaps >300 meV owing to quantum confinement in the absence of electric field. Upon application of electric field by doping with potassium or by close approach of the STM tip, the Stark effect completely closes the bandgap and re-opens it as a conventional gap of 90 meV. The large bandgaps in both the conventional

and quantum spin Hall phases, much greater than the thermal energy $kT = 25$ meV at room temperature, suggest that ultrathin Na_3Bi is suitable for room temperature topological transistor operation.

Two-dimensional Quantum Spin Hall (QSH) insulators are characterized by an insulating interior with bulk bandgap E_g , and topologically protected conducting edge channels that are robust to backscattering by non-magnetic disorder. The QSH effect was first realized in HgTe quantum wells [5] where the small E_g prevents device applications above cryogenic temperatures. This has led to efforts to find new materials with $E_g \gg 25$ meV (thermal energy at room temperature) for room temperature topological electronic devices. Recent reports of QSH insulators bismuthene on SiC ($E_g \sim 0.8$ eV) [6] and monolayer 1T'-WTe₂ ($E_g \sim 50$ meV) [7] are promising, with the quantum spin Hall effect measured in monolayer WTe₂ up to 100K [9]. However, a predicted electric-field effect in WTe₂ has not yet been reported experimentally, and a substantial field-effect in atomically two-dimensional bismuthene is unlikely due to the completely in-plane structure suggesting that any Stark effect would most likely be small.

Ultrathin films of topological Dirac semimetals (TDS) are a promising material class to realise the electric-field tuned topological phase transition, with such a transition predicted in few-layer films of TDS Na_3Bi and Cd_3As_2 [3]. Bulk TDSs are zero-bandgap semimetals with a linear band dispersion in all three dimensions around pairs of Dirac points [10-13], whilst few-layer TDSs are predicted to be non-trivial insulators with bulk bandgaps up to ~ 300 meV for monolayer Na_3Bi [17]. However, experiments on few-layer TDSs are presently lacking, with only 10-15 nm thin films grown to date [14-16]. To unambiguously demonstrate electric field control over the magnitude, electric field-dependence, and topological nature of the bandgap in ultrathin Na_3Bi , we employ two independent experimental techniques. First, we utilize ARPES to directly measure the electronic bandstructure and its modification as a result of doping the surface with potassium to generate an electric field. Second, we use scanning tunnelling spectroscopy (STS), which measures the local density of states (DOS) as a function of energy, to directly probe the energy gap while varying the tip-sample separation and consequently the induced electric field caused by the potential difference between tip and sample. STS also resolves the topological edge state in Na_3Bi at low electric field, demonstrating the topological nature of this phase. These experimental observations are well supported by DFT bandstructure and edge state calculations with and without electric field.

The unit cell of Na_3Bi contains two stacked triple layers in z direction, comprising Na and Bi atoms that form a honeycomb lattice, with interleaved Na atoms as shown in the crystal structures of Fig. 1(a)-(b). One triple layer and two stacked triple layers correspond to monolayer (ML) and bilayer (BL) Na_3Bi respectively as illustrated in Fig. 1(b). The symmetry groups of pristine ML and BL Na_3Bi , and the result of including a Na surface vacancy are summarized in Methods. In Fig. 1(c) STM on few-layer $\text{Na}_3\text{Bi}(001)$ epitaxial films grown via molecular beam epitaxy (MBE) on Si(111) (see Methods M1 for details) reveals coexisting regions of ML and BL Na_3Bi islands that are atomically flat and up to 40 nm in size, along with small areas of bare substrate. Monolayer regions are identified by an additional 0.22 nm distance to the underlying substrate, due to interfacial spacing or structural relaxation which has been observed previously in other atomically thin materials [18]. Figure 1(d) shows the overall band structure of few-layer Na_3Bi films along the M- Γ -K surface directions measured with ARPES at $\hbar\nu = 48$ eV, along with an inset of the 2D Brillouin Zone (BZ). Figure 1(e) shows the second derivative of the spectra in order to enhance low intensity features. This has been overlaid with density functional

theory (DFT) calculations for ML (blue) and BL (green) Na₃Bi showing qualitatively good agreement, consistent with the STM topography which shows coexisting ML and BL regions. Photon-energy dependent ARPES (see Methods M2) demonstrates that the film is electronically 2D, with no dispersion in k_z unlike its bulk or 15 nm thin-film counterparts [10,15]. Depth dependent X-ray photoelectron spectroscopy (XPS) (see Methods M1), revealed no additional components observed in either the Si2p core level corresponding to the Si(111) substrate or the Na and Bi core levels of Na₃Bi, verifying Na₃Bi is free-standing on Si(111).

We first measure the size of the bulk bandgap for ML and BL regions of Na₃Bi by probing the electronic structure with STS, in which the dI/dV spectrum (the differential conductance dI/dV as a function of sample bias V) is proportional to the local density of states at energy $E_F + eV$. Figure 2(a) shows typical dI/dV spectra for ML (red) and BL (black) with bandgaps corresponding to 0.36 ± 0.025 eV and 0.30 ± 0.025 eV respectively (see Methods M3 for details on extracting bandgap values and discussion on the minimal tip-induced band bending). All dI/dV spectra curves in Fig. 2(a) were taken more than 5 nm away from step edges. Figure 2(b) plots the experimental bandgap (blue squares) in comparison to DFT calculated values using the generalized gradient approximation (GGA) for pristine Na₃Bi (black circles) and Na₃Bi layers that contain an Na(2) surface vacancy (red circles) (see Methods for details, with associated bandstructures found in Methods M4). The large bandgap in ML Na₃Bi is consistent with previous calculations[17] and the relatively small change in bandgap from ML to BL observed experimentally is well explained by the DFT calculations that include Na(2) surface vacancies; this vacancy gives rise to a delocalized resonance feature and enhancement of the electronic bandgap [19], resulting in only a small layer-dependent evolution in bandgap. DFT calculations using the GGA method are well known to underestimate the bandgap [20], therefore we employ the more accurate hybrid functional approach with the modified Becke-Johnson (mBJ) potential to better determine the bandgaps for ML Na₃Bi (without vacancies) (see Methods M1 for details). This yields a bandgap of 0.43 eV for ML Na₃Bi, compared to the 0.36 eV obtained for GGA. Whilst, the GGA value is in excellent agreement with the experimental value of 0.36 ± 0.025 eV, this is probably a coincidence due to a reduction in the experimental bandgap as a result of the electric field effect modulation discussed later. The zero field value is likely to be larger and closer to the mBJ value.

To verify the prediction that ML and BL Na₃Bi are large bandgap QSH insulators (see Fig. M4 in Methods) we probe the step edge of these islands to the underlying Si(111) substrate to look for the conductive edge state signature of a QSH insulator. STM topography (Fig. 2(c)) shows a BL Na₃Bi region decorated with Na surface vacancies and a ~ 1.2 nm step edge to the underlying Si substrate, with a small monolayer Na₃Bi protrusion ~ 0.7 nm above the substrate. Figure 2(d) shows dI/dV spectra for BL Na₃Bi far away from the edge (black curve) and at the edge (blue curve). In contrast to the gap in the bulk, the dI/dV spectrum at the edge is quite different, with states filling the bulk gap along with a characteristic dip at 0 mV bias. Similar features observed in other QSH insulators 1T'-WTe₂ [7] and bismuthene [6] have been attributed to one-dimensional (1D) non-trivial edge states and the emergence of a Luttinger liquid [21]. Figure 2(e) shows dI/dV spectra as a function of distance away from the edge, tracing the orange profile in Figure 2(c), demonstrating the extended nature of the edge state feature, with Fig. 2(f) showing that the average dI/dV signal within the bulk bandgap moving away from the edge follows the expected exponential decay for a 1D topological non-trivial state [6].

With ML and BL Na₃Bi verified as large bandgap QSH insulators, we now examine the role of electric field on modifying the size and nature of the bandgap. First, we utilize ARPES to measure the bandstructure after doping the surface with K to generate an electric field. Details on calculating the displacement field are in Methods M5. Figure 3(a)-(d) shows the bandstructure along Γ -K for values of

the electric field of 0.0, 0.72, 1.44 and 2.18 V/nm respectively, with the green and blue dots reflecting the extracted maxima from energy distribution curves (EDC) and momentum distribution curves (MDC; see Methods M5 for details). The right panel in (a)-(d) represents a model of a 2D gapped Dirac system (see Methods M5). In Fig. 3(a) only the hole band is observable, with a hyperbolic band dispersion and asymptotic hole Fermi velocity of $v_F \sim 3 \times 10^5$ m/s. The band dispersion near Γ displays the clear cusp of a band edge indicating a gapped system, with 140 meV separation between the valence band edge and the Fermi energy E_F . The effect of K dosing in Figs. 3(b)-(d) is to *n*-type dope the sample and consequently increase the displacement field. At a displacement field of 0.7 V/nm the separation from the valence band edge to E_F has increased to ~ 257 meV. The bandgap must be at least this amount, consistent with STS, though we cannot determine its exact magnitude since the conduction band lies above E_F (although it can be estimated, see Fig. M7(a)). Upon increasing the displacement field, a Dirac-like electron band emerges with asymptotic Fermi velocity $v_F \sim 10^6$ m/s. The weakness in intensity of the conduction band is most likely due to the different orbital characters of the conduction and valence bands (see Methods M4 and M7 for orbitally resolved DFT bandstructures). At 1.4 V/nm our best estimate of the gap between the two band edges is ~ 100 meV and reduces to ~ 90 meV at 2.2 V/nm (see Methods M5 for calculation). Whilst a significant reduction in bandgap with displacement field clearly occurs, due to the finite energy width of the bands (~ 100 meV) we cannot say definitively whether the gap is fully closed or even reopened again.

To elucidate the effect of an electric field on the electronic structure more clearly, we turn back to measurements made with STM. Here, the tip-sample separation is now varied in order to tune the electric field due to the electrostatic potential difference between the metallic tip and Na₃Bi as illustrated schematically in Fig. 4(a). The electrostatic potential difference is dominated by the difference in work function between the tip and the sample, approximately 1.2 eV (see Methods M6 for calculation). Changes in the bandgap can then be measured in the dI/dV spectra as a function of tip-sample separation and converted to electric field as shown in Fig. 4(b) (details of tip-sample distance calculation and electric field are found in Methods M6). Figure 4(b) shows normalized dI/dV spectra taken on BL Na₃Bi that are offset for clarity (see Methods M6 and Fig. M9 for similar spectra taken on ML Na₃Bi) at various tip-sample separations (electric fields). A large modulation occurs upon increasing the electric field strength, with the bandgap reducing from 300 meV to completely closed (and exhibiting the characteristic V-shape of a Dirac-semimetal) at ~ 1.1 V/nm and then reopening above this to yield a bandgap of ~ 90 meV at ~ 1.2 V/nm. Inset of Fig. 4(b) shows the dI/dV spectra without any offset, highlighting the clear non-zero density of states at the minimum in conductance (i.e. Dirac point) when the bandgap is closed. Figure 4(c) plots the bandgap as a function of electric field for ML and BL Na₃Bi, with both exhibiting a similar critical field where the bandgap is closed and then reopened into the trivial/conventional regime with increasing electric field. DFT calculations also predict such a transition, arising from a Stark effect-induced rearrangement of s- and p-like bands near the gap (see M7 of Methods for full calculation). The projected edge state bandstructures above and below the critical field are shown as insets to Fig. 4(c). Note that due to the difficulty of estimating tip-sample distance, the electric field magnitude may include a systematic error as large as 50%, however the trend of gap size with electric field is correct.

By combining ARPES and STS, we have demonstrated that monolayer and bilayer Na₃Bi are quantum spin Hall insulators with bulk bandgaps above 300 meV, offering the potential to support dissipationless transport of charge at room temperature. An electric-field tunes the phase from topological to conventional insulator with bandgap of ~ 90 meV due to a Stark effect-driven transition. This bandgap modulation of more than 400 meV is larger than has been achieved in atomically thin semiconductors such as bilayer graphene [22,23] and similar to phosphorene [24], and may be useful in optoelectronic

applications [25] in the mid-infrared. Na_3Bi is chemically inert in contact with silicon, and the electric fields required to induce the topological phase transition are typically below the breakdown field of conventional dielectrics, meaning that future experiments that measure the ballistic edge current turn on/off along the film edges may be possible. These aspects make ultrathin Na_3Bi a promising platform for realising new forms of electronic switches based on topological transistors for low-energy logic circuits.

References:

- [1] X. Qian, J. Liu, L. Fu, J. Li, Quantum spin Hall effect in two-dimensional transition metal dichalcogenides, *Science* 346, 1344 (2014)
- [2] J. Liu, T. H. Hsieh, P. Wei, W. Duan, J. Moodera, L. Fu, Spin-filtered edge states with an electrically tunable gap in a two-dimensional topological crystalline insulator, *Nature Materials* 13, 178 (2014)
- [3] H. Pan, M. Wu, Y. Liu, S. A. Yang, Electric control of topological phase transitions in Dirac semimetal thin films, *Scientific Reports* 5, 14639 (2015)
- [4] W. G. Vandenberghe, M. V. Fischetti, Imperfect two-dimensional topological insulator field-effect transistors, *Nature Communications* 8, 14184 (2017)
- [5] M. König, S. Wiedmann, C. Brüne, A. Roth, H. Buhmann, L. W. Molenkamp, X.-L. Qi, S.-C. Zhang, Quantum Spin Hall Insulator State in HgTe Quantum Wells, *Science* 318, 766 (2007)
- [6] F. Reis, G. Li, L. Dudy, M. Bauernfeind, S. Glass, W. Hanke, R. Thomale, J. Schäfer, R. Claessen, Bismuthene on a SiC substrate: A candidate for a high-temperature quantum spin Hall material, *Science* 357, 287 (2017)
- [7] S. Tang, C. Zhang, D. Wong, Z. Pedramrazi, H.-Z. Tsai, B. Moritz, M. Claassen, H. Ryu, S. Kahn, J. Jiang, H. Yan, M. Hashimoto, D. Lu, R. G. Moore, C. Hwang, C. Hwang, Z. Hussain, Y. Chen, M. M. Ugeda, Z. Liu, X. Xie, T. P. Devereaux, M. F. Crommie, S.-K. Mo, Z.-X. Shen, Quantum Spin Hall State in Monolayer $1\text{T}'\text{-WTe}_2$, *Nature Physics* 13, 683 (2017)
- [8] Z. Fei, T. Palomaki, S. Wu, W. Zhao, X. Cai, B. Sun, P. Nguyen, J. Finney, X. Xu, D. H. Cobden, Edge conduction in monolayer WTe_2 , *Nature Physics* 13, 677-682 (2017)
- [9] S. Wu, V. Fatemi, Q. D. Gibson, K. Watanabe, T. Taniguchi, R. J. Cava, P. Jarillo-Herrero, Observation of the quantum spin Hall effect up to 100 kelvin in a monolayer crystal, *Science* 359, 76 (2018)
- [10] Z. K. Liu, B. Zhou, Y. Zhang, Z. J. Wang, H. M. Weng, D. Prabhakaran, S.-K. Mo, Z. X. Shen, Z. Fang, X. Dai, Z. Hussain, Y. L. Chen, Discovery of a Three-Dimensional Topological Dirac Semimetal, Na_3Bi , *Science* 343, 864 (2014)
- [11] Z. Wang, Y. Sun, X.-Q. Chen, C. Franchini, G. Xu, H. Weng, X. Dai, and Z. Fang, Dirac semimetal and topological phase transitions in A_3Bi ($\text{A}=\text{Na}, \text{K}, \text{Rb}$), *Phys. Rev. B* 85, 195320 (2012)
- [12] Z. K. Liu, J. Jiang, B. Zhou, Z. J. Wang, Y. Zhang, H. M. Weng, D. Prabhakaran, S.-K. Mo, H. Peng, P. Dudin, T. Kim, M. Hoesch, Z. Fang, X. Dai, Z. X. Shen, D. L. Feng, Z. Hussain, and Y. L. Chen, A stable three-dimensional topological Dirac semimetal Cd_3As_2 , *Nature Materials* 13, 677 (2014)
- [13] S. Borisenko, Q. Gibson, D. Evtushinsky, V. Zabolotnyy, B. Büchner, and R. J. Cava, Experimental realization of a three-dimensional Dirac semimetal, *Phys. Rev. Lett.* 113, 027603 (2014)
- [14] J. Hellerstedt, M. T. Edmonds, N. Ramakrishnan, C. Liu, B. Weber, A. Tadich, K. M. O'Donnell, S. Adam, and M. S. Fuhrer, Electronic properties of high-quality epitaxial topological Dirac semimetal thin films, *Nano Letters* 16, 3210 (2016)
- [15] Y. Zhang, Z. Liu, B. Zhou, Y. Kim, Z. Hussain, Z. X. Shen, Y. Chen, Y. and S.-K. Mo, Molecular beam epitaxial growth of a three-dimensional topological Dirac semimetal Na_3Bi , *Applied Physics Letters* 105, 031901 (2014)

- [16] T. Schumann, L. Galletti, D. A. Kealhofer, H. Kim, M. Goyal, S. Stemmer, Observation of the Quantum Hall Effect in Confined Films of the Three-Dimensional Dirac Semimetal Cd_3As_2 , *Phys. Rev. Lett.* 120, 016801 (2018)
- [17] C. Niu, P. M. Buhl, G. Bihlmayer, D. Wortmann, Y. Dai, S. Blügel, Y. Mokrousov, Robust dual topological character with spin-valley polarization in a monolayer of the Dirac semimetal Na_3Bi , *Phys. Rev. B* 95, 075404 (2017)
- [18] J. Wu, H. Yuan, M. Meng, C. Chen, Y. Sun, Z. Chen, W. Dang, C. Tan, Y. Liu, J. Yin, Y. Zhou, S. Huang, H. Q. Xu, Y. Cui, H. Y. Hwang, Z. Liu, Y. Chen, B. Yan, H. Peng, High electron mobility and quantum oscillations in non-encapsulated ultrathin semiconducting $\text{Bi}_2\text{O}_2\text{Se}$, *Nature Nano* 12, 530 (2017)
- [19] M. T. Edmonds, J. L. Collins, J. Hellerstedt, Yudhistira, L. C. Gomes, J. N. B. Rodrigues, S. Adam, M. S. Fuhrer, Spatial charge inhomogeneity and defect states in topological Dirac semimetal thin films of Na_3Bi , *Science Advances* 3, 6661 (2017)
- [20] J. P. Perdew, W. Yang, K. Burke, Z. Yang, E. K. U. Gross, M. Scheffler, G. E. Scuseria, T. M. Henderson, I. Y. Zhang, A. Ruzsinszky, H. Peng, J. Sun, E. Trushin, A. Görling, Understanding band gaps of solids in generalized Kohn-Sham theory, *PNAS* 114,2801 (2017)
- [21] J. Voit, One-dimensional fermi liquids, *Reports on Progress in Physics* 58, 977 (1995)
- [22] T. Ohta, A. Bostwick, T. Seyller, K. Horn, E. Rotenberg, Controlling the Electronic Structure of Bilayer Graphene, *Science* 313, 951-954 (2006)
- [23] Y. Zhang, T.-T. Tang, C. Girit, Z. Hao, M. C. Martin, A. Zettl, M. F. Crommie, Y. Ron. Shen. F. Wang, Direct observation of a widely tunable bandgap in bilayer graphene, *Nature* 459, 820 (2009)
- [24] B. Deng, V. Tran, Y. Xie, H. Jiang, C. Li, Q. Guo, X. Wang, H. Tian, S. J. Koester, H. Wang, J. J. Cha, Q. Xia, L. Yang, F. Xia, Efficient electrical control of thin-film black phosphorus bandgap, *Nature Comms* 8, 14474 (2017)
- [25] L. Ju, L. Wang, T. Cao, T. Taniguchi, K. Watanabe, S. G. Louie, F. Rana, J. Park, J. Hone, F. Wang, P. L McEuen, Tunable excitons in bilayer graphene, *Science* 358, 907 (2017)

Acknowledgements

M. T. E. is supported by ARC DECRA fellowship DE160101157. M. T. E., J. L. C., C. L., and M. S. F. acknowledge funding support from CE170100039. J. L. C., J. H and M. S. F. are supported by M. S. F.'s ARC Laureate Fellowship (FL120100038). M. T. E. and A. T. acknowledge travel funding provided by the International Synchrotron Access Program (ISAP) managed by the Australian Synchrotron, part of ANSTO, and funded by the Australian Government. M. T. E. acknowledges funding from the Monash Centre for Atomically Thin Materials Research and Equipment Scheme. S. Y. and W. W. acknowledge funding from Singapore MOE AcRF Tier 2 (Grant No. MOE2015-T2-2-144). This research used resources of the Advanced Light Source, which is a DOE Office of Science User Facility under contract no. DE-AC02-05CH11231. Part of this research was undertaken on the soft X-ray beamline at the Australian Synchrotron, part of ANSTO.

Author Statements

M. T. E., J. L. C., and M. S. F. devised the STM experiments. M. T. E. devised the ARPES and XPS experiments. M. T. E. and J. L. C. performed the MBE growth and STM/STS measurements at Monash University. J. H. assisted with the experimental setup at Monash University. M. T. E., J. L. C. and A. T. performed the MBE growth and ARPES measurements at Advanced Light Source with the support from H. R., S. T. and S. K. M.. The MBE growth and XPS measurements at the Australian Synchrotron were performed by M. T. E., J. L. C. A. T., J. H., C. L. The DFT calculations were performed by L. C. G, J. N. B. R., W. W. and S. Y.. S. A. assisted with the theoretical interpretation of the data. J. L. C., M.

T. E., and M. S. F. composed the manuscript. All authors read and contributed feedback to the manuscript.

Reprints and permissions information is available at www.nature.com/reprints

The authors declare no competing interests.

Correspondence and requests for materials should be addressed to mark.edmonds@monash.edu

Main Figure Legends

Figure 1. Characterization of epitaxial few-layer Na₃Bi and overall electronic structure from ARPES. (a) Top and (b) side view of the Na₃Bi unit cell. A monolayer (ML) has one triple-layer (Na-NaBi-Na) unit, and a bilayer (BL) has two such units. (c) Large area (200 nm x 200 nm) topographic STM image (bias voltage $V = 2.0$ V and tunnel current $I = 120$ pA) of few layer Na₃Bi on Si(111). The different regions are colour coded with ML (dark grey), BL (light grey) and Si(111) (dark blue). (d) Overall band structure along the M- Γ -K directions measured with ARPES at $h\nu = 48$ eV. Inset shows the 2D Brillouin zone. (e) The second derivative of (d) enhances low intensity features. Overlaid blue and green curves are calculated DFT bandstructures for ML and BL Na₃Bi respectively.

Figure 2. Bandgap in ML and BL Na₃Bi and edge state behaviour. (a) Normalized dI/dV spectra displayed on a logarithmic plot corresponding to ML (red) and BL (black) Na₃Bi. The conduction and valence band edges are reflected by the sharp onset of dI/dV intensity. Details are found in Methods M3. (b) Evolution of the bandgap as a function of layer thickness determined from dI/dV spectra (blue squares), DFT calculations utilizing the GGA functional on pristine Na₃Bi (black circles) and with an Na(2) vacancy (red circles), and DFT calculations utilizing the mBJ potential (green diamonds) (see Methods M1 for details). (c) Upper: STM topography of a region of BL Na₃Bi (grey), and the underlying Si(111) substrate (red). The orange line reflects the region over which the dI/dV measurements were performed in (e), and the green line extends the profile across the pinhole step. Lower: Cross-section through the pinhole overlaid with the orange and green line profiles. (d) dI/dV spectra taken near the step edge of BL Na₃Bi to Si(111) substrate (blue) and in the bulk of BL Na₃Bi (black). (e) dI/dV colour map taken at and then moving away from the step edge where the dashed vertical lines reflect the spectra shown in (d) and the horizontal lines represent the averaged dI/dV signal within the bulk bandgap region that is shown in (f). (f) Corresponding intensity profile of dI/dV in the bulk gap showing the exponential decay away from the step edge, where the orange trace represents the topography height profile and red trace represents the average dI/dV magnitude within the bulk bandgap, indicated by the horizontal dashed region of (e).

Figure 3. Bandstructure modulation in ARPES in ML and BL Na₃Bi using K dosing. (a)-(d) ARPES intensity plots showing the evolution of the band dispersion with K dosing, where at each dose the left panel shows the ARPES spectra, the points are the maxima extracted from MDC (green) and EDC (blue); and the right panel shows fits of the maxima to hyperboles (solid lines) along with the linear asymptotes (dashed lines; see Methods M5 for details). (a) Before *in-situ* K dosing. The hole band is located ~ 140 meV below E_F ; (b) K dosing equivalent to a 0.72 V/nm displacement field; the hole band is now 257 meV below E_F ; (c) K dosing equivalent to a 1.44 V/nm displacement field has *n*-type doped the system to an extent that an electron band has now emerged, separated from the hole band by ~ 100 meV; (d) K dosing equivalent to 2.18 V/nm displacement field results in further *n*-type doping with the band separation 90 meV.

Figure 4. Electric-field induced bandgap modulation of ML and BL Na₃Bi in STM. (a) Schematic representation of a metallic tip at a fixed distance ‘s’ above the surface of Na₃Bi, with the difference in work function generating a localized electric field in the vicinity of the tip (see Methods section M6 for determining tip and sample work functions). (b) Individual dI/dV spectra taken on BL Na₃Bi at different tip-sample separations (electric fields) as labelled on the figure, where A, B and C correspond to tip height (electric fields) of 1.45 nm (0.828 V/nm), 1.075 nm (1.12 V/nm), and 1.02 nm (1.18 V/nm) respectively. The spectra have been normalized and offset for clarity. The inset shows the spectra without being offset, highlighting the non-zero conductance at the conductance minima. (c) Bandgap extracted from dI/dV spectra as a function of electric field for ML (red squares) and BL (black triangles). At a critical field of ~ 1.12 V/nm the system is no longer gapped, above this a bandgap reopens in the conventional regime. The orange and purple shaded regions represent guides to the eye. Insets represent DFT projected edge state bandstructures below and above the critical field (see Methods M7 for full calculation). A, B and C mark the points extracted from the respective spectra in Fig. 4(b).

Methods

M1. Growth of few-layer Na₃Bi on Si(111), experimental parameters and characterization via RHEED, LEED and XPS

M2. Band dispersion in k_z from Photon energy-dependent ARPES

M3. Bandgap extraction from scanning tunneling spectra

M4. DFT Calculations for Na(2) vacancy Na₃Bi layers and Z2 calculations

M5. ARPES band dispersion fitting and displacement field calculations

M6. dI/dV normalization and calculating tip-sample separation and electric field

M7. DFT Calculations of electric field induced topological phase transition

M8. Summary of crystalline symmetries for ML and BL Na₃Bi

M1. Growth of few-layer Na₃Bi on Si(111), experimental parameters and characterization via RHEED, LEED and XPS

1.1 Growth of few-layer Na₃Bi on Si(111)

Ultra-thin Na₃Bi thin films were grown in ultra-high vacuum (UHV) molecular beam epitaxy (MBE) chambers and then immediately transferred after the growth under UHV to the interconnected measurement chamber (i.e. Createc LT-STM at Monash University, Scienta R-4000 analyser at Advanced Light Source and SPEC Phoibos 150 at Australian Synchrotron). To prepare an atomically flat substrate, a *p*-type Si(111) wafer was flash annealed to 1250°C in order to achieve a (7 x 7) surface reconstruction (this was achieved via direct current heating at Monash University and the Australian Synchrotron, and via electron bombardment heating at the Advanced Light Source).

For Na₃Bi film growth effusion cells were used to simultaneously evaporate elemental Bi (99.999%) in an overflux of Na (99.95%) with a Bi:Na flux ratio not less than 1:10, calibrated by quartz microbalance. During growth the substrate temperature was between 300°C-330°C for successful crystallization. At the end of the growth the sample was left at the growth temperature for 10 min in an Na overflux to improve the film quality before cooling to room temperature.

1.2 Experiment Parameters

STM/STS Measurements:

STM/STS measurements were performed in a Createc LT-STM operating at 5K. A PtIr tip was prepared and calibrated using an Au(111) single crystal and confirming the presence of the Shockley surface state at -0.5V and flat LDOS near the Fermi level before all measurements. After measurements on few-layer Na₃Bi were completed the Au(111) sample was re-measured to confirm the tip had not

significantly changed and still exhibited flat local density of states (LDOS) near the Fermi level. STM differential conductance measurements (dI/dV) were measured using a 5 mV AC excitation voltage (673 Hz) that was added to the tunnelling bias. Differential conductance measurements were made under open feedback conditions with the tip in a fixed position above the surface. Data was prepared and analysed using MATLAB and IGOR Pro.

Angle resolved photoemission spectroscopy (ARPES) measurements:

ARPES measurements were performed at Beamline 10.0.1 of the Advanced Light Source (ALS) at Lawrence Berkeley National Laboratory, USA. Data was taken using a Scienta R4000 analyzer at 20 K sample temperature. The total energy resolution was 20-25 meV depending on the beamline slit widths and analyser settings, and the angular resolution was 0.2° . This resulted in an overall momentum resolution of $\sim 0.01 \text{ \AA}^{-1}$ for photoelectron kinetic energies measured, with the majority of the measurements performed at $h\nu = 48 \text{ eV}$ and 55 eV . Doping of the Na_3Bi films was performed via in-situ K dosing from a SAES getter source in UHV. Dosing was performed at a temperature of 20 K to avoid K clustering.

XPS Measurements:

XPS measurements were performed at the Soft X-ray Beamline of the Australian Synchrotron using a SPECS Phoibos-150 spectrometer at room temperature. The Bi 5d and Na 2p of the Na_3Bi , as well as the Si 2p of the Si(111) substrate were measured at photon energies of 100 eV, 350 eV, 800 eV and 1487 eV. This ensured surface sensitivity for the low photon energy scans at 100 eV, with the higher photon energies used to characterize the depth dependence of the core levels, in particular whether there was any chemical bonding between the Na_3Bi film and the Si(111) substrate. The binding energy scale of all spectra are referenced to the Fermi energy (E_F), determined using either the Fermi edge or 4f core level of an Au reference foil in electrical contact with the sample. Core level spectra were analysed using a Shirley background subtraction. Kelvin probe measurements to determine the work function of Na_3Bi were also performed on this system.

Density Functional Theory (DFT) Calculations:

First-principles calculations based on density-functional theory (DFT) are used to obtain electronic band structures of monolayer and bilayer Na_3Bi , with and without Na(2) vacancies. This was achieved using the projector augmented wave (PAW) method [26] with calculations implemented in Quantum ESPRESSO code and the Vienna ab initio Simulation Package (VASP). The generalized gradient approximation (GGA) using the PBE functional [27] for the exchange-correlation potential were adopted. The plane-wave cutoff energy was set to be 400 eV. The Brillouin zone sampling was performed by using k grids with a spacing of $2\pi \times 0.02 \text{ \AA}^{-1}$ within a Γ -centered sampling scheme. For all calculations, the energy and force convergence criteria were set to be 10^{-5} eV and 10^{-2} eV/\AA , respectively. For the ML and BL Na_3Bi calculations with Na surface vacancy there is 1 Na vacancy per 2×2 supercell. For the Na_3Bi layers, we used a vacuum region of thickness larger than 15 \AA thickness to eliminate the artificial interaction between the periodic images. The edge states were studied by constructing the maximally localized Wannier functions [28] and by using the iterative Green's function method [29] as implemented in the WannierTools package [30]. More accurate calculations of the bandgap for ML and BL Na_3Bi (without Na vacancies) were performed via a more accurate hybrid functional approach using the modified Becke-Johnson potential [31-33].

1.3 Characterization via RHEED, LEED and XPS

In order to confirm that the few-layer films of Na_3Bi are high quality and epitaxial over large areas we performed reflection high-energy electron diffraction (RHEED), low energy electron diffraction (LEED)

and X-ray photoelectron spectroscopy (XPS) as shown in Fig. M1. Figure M1(a) shows the characteristic RHEED pattern for Si(111) 7×7 reconstruction along $\bar{\Gamma} - \bar{M}$, whilst Fig. M1(b) shows the RHEED pattern for few-layer Na₃Bi along $\bar{\Gamma} - \bar{K}$, consistent with RHEED reported on films of 15 unit cell thickness, where the lattice orientation of Na₃Bi is rotated 30° with respect to the Si(111) substrate [15]. Figure M1(c) shows the 1×1 LEED pattern consistent with growth of Na₃Bi in the (001) direction. The sharpness of the spots and absence of rotational domains indicates high-quality single crystal few-layer Na₃Bi over a large area. Figure M1(d) shows the Bi 5d and Na 2p core levels of a few-layer Na₃Bi film taken at $h\nu = 100$ eV, with the peak positions consistent with published results on 20 nm film and bulk Na₃Bi [10, 15, 34].

To rule out reaction of Na₃Bi with the Si substrate, we performed depth-dependent XPS (by varying the photon energy in order to increase the kinetic energy of emitted photoelectrons, as a result increasing the mean free path) to examine the Na₃Bi and Si(111) interface. The Na and Bi core levels exhibited no additional components (data not shown). Figure M1(e) shows XPS of the Si 2p core level (reflecting the substrate) at photon energy $h\nu = 350$ eV (left panel) and $h\nu = 850$ eV (right panel). In each panel the black curve represents the Si 2p core level of the bare Si(111) 7×7 and the red curve represents the Si 2p core level with few-layer Na₃Bi grown on top. In each case, the spectra have been normalized to the maximum in intensity and energy-corrected (to account for the small interfacial charge transfer that occurs) in order to overlay the core levels. The spectra have been offset for clarity. It is clear there is negligible change to the Si 2p core level after Na₃Bi growth, with no additional components or significant broadening arising, verifying that Na₃Bi is free-standing on Si(111). This is consistent with the fact that our ARPES measurements on ultrathin Na₃Bi showed no features with the Si(111) 7×7 symmetry.

M2. Band dispersion in k_z from Photon energy-dependent ARPES

Photon energy-dependent ARPES can be utilized to determine whether a material possesses a 3D band dispersion, i.e. the binding energy E_B depends not only on in-plane wavevectors k_x and k_y , but also on out-of-plane wavevector k_z . To determine the momentum perpendicular to the surface requires measuring energy distribution curves as a function of the photon-energy in order to measure E_B vs k_z , using the nearly free-electron final state approximation [35,36]:

$$k_z = \sqrt{\frac{2m}{\hbar^2} (E_k + V_0 - E_k \sin^2 \theta)} \quad (2.1)$$

where θ is the emission angle, m is the effective mass of electrons, V_0 is the inner potential (reflecting the energy difference between the bottom of the valence band to the vacuum level) and E_k is the kinetic energy of the emitted photoelectrons where $E_k = h\nu - \Phi - E_B$ with $h\nu$ the photon energy, Φ the work function and E_B the energy. At normal emission (i.e. $\theta = 0$) equation (2.1) simplifies to

$$k_z = \sqrt{\frac{2m}{\hbar^2} (E_k + V_0)} \quad (2.2)$$

Therefore, using (2.2) and measuring energy distribution curves at normal emission as a function of photon energy we can directly measure E_B vs k_z assuming an inner potential, $V_0 = 12.5$ eV for Na₃Bi determined in [10].

Figure M2, shows a colour plot of k_z as a function of binding energy (and reflects energy distribution curves taken at normal emission for photon energies between 45-55 eV. A flat band is observed near 0 eV (the Fermi energy) and represents the valence band maximum.

This band possesses no dispersion in k_z (i.e. no bulk band dispersion), verifying that few-layer Na_3Bi is indeed electronically 2D, unlike its thin-film and bulk counterparts.

M3. Bandgap extraction from scanning tunneling spectra and tip-induced band bending

3.1 Bandgap extraction

Determining the bulk electronic bandgap of mono- and bilayer Na_3Bi was achieved by performing scanning tunnelling spectroscopy (dI/dV as a function of sample bias V) more than 5 nm away from step edges. The valence and conduction band edges in the local density of states (LDOS) are defined as the onset of differential conductance intensity above the noise floor. Due to the large variation in dI/dV signal near a band edge, it was useful to plot the logarithm of the dI/dV curves for accurate band gap determination as shown in Figure M3 (a) and (b).

For measurements involving tuning the electric field by varying the tip-sample distance dI/dV spectra were taken over a wide range of tunnelling currents (0.01-1 nA), resulting in large changes in signal at band edges and a change in the relative magnitude of signal to noise. In order to unambiguously determine the magnitude of the gap without reference to the noise magnitude, we adopted the following procedure. Spectra were normalized to a relatively featureless point in the LDOS away from the band edge onset. The dI/dV signal corresponding to a bias of -400 meV was chosen for normalization, after the normalization procedure was completed for all spectra, we take the band edges as the point at which the dI/dV has fallen to 0.01 of the normalized value. We find that this definition closely corresponds to the onset of conductance above the noise floor (see Fig. M3(c)). Normalization was also performed at -300 meV, 300 meV and 400 meV with only a small variation <15 meV observed, due to the sharp onset in conductance in both the valence and conduction bands. Accounting for error in the normalization and the tip-induced band bending discussed below, yields an error in determining the gap magnitude of ± 25 meV.

3.2 Tip-induced band bending

Tip-induced band bending (TIBB) effects have the potential to overestimate the size of the electronic bandgap due to unscreened electric fields and can strongly influence the interpretation of STM data. The absence/presence of TIBB is usually verified by performing dI/dV spectra at different initial current setpoints (different tip-sample separations). In the absence of TIBB there will be negligible change in the band edges of the spectra, however, if the spectra are strongly influenced by TIBB increasing the current setpoint (reducing tip-sample separation) will lead to increased band bending, and overestimation of the bandgap [37]. As shown in Fig. 4(b) the exact opposite is observed for few-layer Na_3Bi , in this case the bandgap becomes smaller, then closes and then reopens upon increasing the current (and consequently electric field), and is clearly not consistent with TIBB. However, we also cannot rule out whether the dI/dV spectra taken at low currents (low fields) (as shown in Fig. 2) are intrinsic or free from TIBB.

In order to estimate the effects of tip-induced band bending (TIBB) we first adopt a model based on a uniformly charged sphere [37] with the analytic expression for the difference ϕ_{BB} between the apparent (measured) and actual energy position of a spectral feature (e.g. band edge) due to TIBB:

$$\phi_{BB}(V_b, r, h, \varepsilon) = \frac{1}{1 + \varepsilon \frac{h}{r}} (eV_b - W_0) \quad (3.1)$$

where ε is the dielectric constant, h the tip height, r the tip radius and W_0 the work function difference between sample and tip (i.e. $W_0 = W_{\text{sample}} - W_{\text{tip}}$). We use $h = 1.5$ nm and $W_0 = -1.2$ eV (taken from calculations in Section M6) and assume a tip radius, $r = 25$ nm. For the static dielectric constant we use the value for bulk Na₃Bi, $\varepsilon = 120$ [14]. Whilst, the dielectric constant in ML and BL Na₃Bi could be very different, the bulk value is currently the only available value and used as a rough estimate. Figure M3(d) plots ϕ_{BB} as a function of bias voltage calculated from eqn. (3.1). The correction factor for tip-induced band bending is given by $1/(1 - \frac{\partial \phi}{\partial V})$, which yields 1.13 for Na₃Bi.

The uniformly charged sphere model is known to overestimate TIBB by almost a factor of 2 when more detailed modelling that incorporates charge redistribution is taken into account [37]. Therefore, we adopt the image charges method for a charged sphere in front of a dielectric sample (see Appendix from Ref. 37). In this case the TIBB band bending expression is replaced by

$$\phi_{BB}(V_b, r, h, \varepsilon) = F(r, h, \varepsilon)(eV_b - W_0) \quad (3.2)$$

where F is the ratio of the electrical potential on the tip surface and at the point of the sample closest to the tip. For $h = 1.5$ nm, $r = 25$ nm and $\varepsilon = 120$ we find that $F = 0.064$, yielding a TIBB correction factor of 1.07, meaning our best estimate is that the measured bandgap of ultra-thin Na₃Bi includes a systematic overestimation due to TIBB of 7%. For ML and BL Na₃Bi with bandgaps of 360 meV and 300 meV this corresponds to 25 meV and 21 meV respectively. Because this is comparable to the random error of ± 25 meV as discussed in 3.1, we have not corrected for TIBB.

M4. DFT Calculations for Na(2) vacancy Na₃Bi layers and Z₂ calculations

The calculated band structures of Na₃Bi monolayer and bilayer with Na(2) vacancy including spin-orbital coupling (SOC) are displayed in Fig. M4 (b) and (g) respectively. Bandgaps of 0.30 eV (0.28 eV) and 0.22 eV (0.16 eV) are obtained for monolayer (without structural relaxation) and bilayer respectively, with the band gaps obtained from DFT using the Quantum Espresso code and the value obtained from the VASP package in brackets. The non-trivial topological character can be intuitively observed from the orbital components of the band edge states. As shown in Fig. M4 (c, h) without spin-orbit coupling (SOC) for ML and BL respectively, the CBM is mainly contributed by Na-*s* and Bi-*s* orbitals, whereas the VBM is mainly from the Bi-*p_x/p_y* orbitals, showing a normal band ordering. After including SOC (d, i) for ML and BL respectively, the band ordering is inverted at Γ , with *p*-orbitals at the CBM above the *s*-orbitals at VBM. This SOC-induced band inversion marks a topological nontrivial phase, which indicates that both ML and BL Na₃Bi are nontrivial 2D topological insulators. The edge state spectrum is shown in Fig. M4 (e) for ML and (j) for BL. The projected 1D Brillouin zone is shown in (a). One can clearly observe a Kramers pair of topological edge states. To prove these systems are non-trivial we determine the topological invariant of both systems. This is done by employing the Wilson loop method [38,39], in which one traces the evolution of the Wannier function centers, as plotted in Fig. 1(f) and 1(k). From the calculation, we confirm that both the monolayer and the bilayer Na₃Bi with and without Na(2) vacancy are topologically nontrivial with the invariant $Z_2 = 1$.

M5. ARPES band dispersion fitting and displacement field calculations

5.1 Extracting and fitting the ARPES band dispersion of few-layer Na₃Bi:

Energy dispersion curves (EDCs) and momentum dispersion curves (MDCs) are slices through constant-momentum and constant-energy of the photoemission spectra (such as Fig. M5 (a)) along high-symmetry directions (M - Γ - M) or (K - Γ - K) respectively. Band energy and momentum coordinates are extracted by Gaussian fitting of the photoemission intensity on a flat background (as shown in Fig. M5(b) and (c) by the blue circles). We find that band edges are extracted more reliably from EDCs, whilst MDCs peak positions are used at larger binding energies where clearly distinct peaks can be resolved (see left panel of Fig. M5(b)).

The measured bands are observed to fit hyperbolae as shown in Figure M5(d), as expected of gapped Dirac systems. Fits of the bands to a parabola are much poorer, as shown in Fig. M5(e). In order to accurately model the band dispersion of a 2D gapped Dirac system we use a bi-partite model for the valence (p) and conduction (n) bands that assumes the form

$$(E_{B,i} - D)^2 = \Delta_i^2 + \hbar^2 v_{F,i}^2 (k + k_0)^2, i \in p, n \quad (5.1)$$

where $\Delta = \Delta_n + \Delta_p$ represents the energy gap, $v_{F,i}$ the asymptotic Fermi velocities at large momenta, and D a doping or energy-shift of the bands.

The velocities $v_{F,i}$ measured for the valence and conduction bands for both films are nearly independent of K dosing, with near-isotropic dispersion in k_x, k_y (also shown in Fig. M6). Hence we take $v_{F,n}$ and $v_{F,p}$ to be a global fit parameter, with best fit values $v_{F,n} \approx 1 \times 10^6 \text{ m/s}$; $v_{F,p} \approx 3 \times 10^5 \text{ m/s}$.

We then fit the valence band photoemission i.e. the negative solution for (5.1) using the global $v_{F,p}$ parameter, allowing us to determine Δ_p and D as a function of K-dosing. A monotonic increase of D with K-dosing is observed as expected, reflecting the shift of the valence band to larger binding energy.

The photoemission intensity of the electron band is two orders of magnitude less than that of the valence band – possibly due to the different orbital characters of the two bands resulting in a lower intensity due to matrix element effects. Due to the large band gap of few-layer Na_3Bi , the conduction band lies well above the Fermi level in the as-grown film, meaning that significant charge transfer from K-dosing is needed to n -type dope the film in order to observe the conduction band. As such the fitting parameter Δ_n for the electron bands can only be determined once the conduction band is resolvable below E_F , and in addition further seen to match with the valence band determined value for D . Values for $\Delta_{n,p}$ as a function of electric displacement field are addressed in 5.3

5.2 Mapping from K-deposition to space-charge generated electric displacement field:

Potassium deposited on the Na_3Bi surface donates electrons leaving a positive K^+ ion behind, producing a uniform planar charge density. This is equivalent to a parallel plate capacitor, allowing the electric displacement field, \vec{D} to be calculated across the Na_3Bi film using Gauss' law via:

$$\vec{D} = \frac{\vec{E}}{\epsilon} = \frac{eQ}{\epsilon_0} = \frac{e\Delta n}{\epsilon_0} \quad (5.2)$$

with Q representing the total charge transferred due to potassium doping, i.e. $Q = \Delta n$.

The charge transfer to the system cannot be directly inferred when a Fermi surface cannot be clearly resolved, so our calculations make use of the conduction band Fermi surface that becomes distinct after 15 minutes of K-dosing. As seen in Figure M6(a), the n -type Fermi surface is a nearly isotropic Dirac cone. By measuring k_F as a function of K-dosing either from EDCs or a Fermi surface map as in Fig. M6(b), the charge density can be directly calculated using

$$n(k_F) = \frac{g}{4\pi} k_F^2, \quad (5.3)$$

where a band degeneracy of $g = 4$ can be taken for Dirac systems [14]. The charge density $n(k_F)$ is also consistent with the assumption of a Dirac dispersion centred at D , i.e. $k_F = D/\hbar v_F$.

The change in $n(k_F)$ as a function of K-dosing is approximately $2 \times 10^{12} \text{ cm}^{-2}$ between consecutive K-dosing until the 50-minute mark (where charge saturation occurs). By assuming that in this regime every K atom donates one electron and a constant dose rate we can extrapolate the total $n(k_F)$ back to the doping of the as-grown film growth. For the as-grown film this corresponds to a p -type doping of $4 \times 10^{12} \text{ cm}^{-2}$. From this as-grown doping we can then calculate the electric displacement field using eqn. 5.2, as shown on the right hand axis of Figure M6(c).

5.3 Electric displacement field dependence of few-layer Na_3Bi bandstructure from ARPES:

Next we map the calculated $\Delta_{n,p}$ (which reflects the size of the bandgap) at different K-dosing to a corresponding electric displacement field as shown in Figure M7(a). The purple circles in (a) represent where $\Delta_{n,p}$ are directly extracted from the bi-partite model to the experimental data. At low displacement field, where the conduction band is still above the Fermi level, we cannot directly obtain a value for Δ_n . As such we estimate the size of Δ_n at these low displacement fields using the ratio $\frac{\Delta_p + \Delta_n}{\Delta_p} \approx 1.4$, which is directly obtained from the purple points. For the as-grown sample this yields a value of $\sim 320 \text{ meV}$, which given we cannot directly measure the conduction band edge is in reasonable agreement with the experimental result from STS, and the theoretical DFT value. The reduction in bandgap is consistent with the independently measured gap-closing from STS in Fig. 4(c) of the main manuscript, with the relative energy separation of the electron and valence bands narrowing monotonically with increasing field. When the estimated bandgap $\Delta = \Delta_n + \Delta_p$ becomes as small as 100 meV (corresponding to displacement fields $> 1.5 \text{ V/nm}$), it is comparable to the intrinsic energy broadening of the bands (particularly the valence band). Therefore, we cannot definitely conclude from ARPES measurements whether the band gap completely closes after this point or is re-opened again.

M6. Calculating tip-sample separation and electric field

In scanning tunnelling microscopy for a simple square barrier the tunnelling current (in atomic units) follows

$$I_t = I_0 e^{-2(z-z_0)\sqrt{2\Phi}} \quad (6.1)$$

where Φ is the work function of the energy barrier and z and z_0 the tip and sample positions respectively, such that the distance between tip and sample is $s = z - z_0$. This allows the work function of the barrier to be obtained by measuring the tunnelling current as a function of tip position, then extracting the slope of $\ln(I_t)/z$:

$$\frac{d\ln(I)}{dz} = -2\sqrt{2\Phi} \quad (6.2)$$

Figure M8 shows logarithmic plots of the tunnelling current as a function of relative distance for (a) Au(111) (bias 500 mV) and (b) thin film Na₃Bi (bias -300 mV) where the absolute current is plotted. For Au(111) the characteristic exponential dependence of $I(z)$ (straight line on the semi-log plot) is observed with current increasing from 0.01 nA to 10 nA by moving the tip 3 Å closer to the surface. However, it is immediately clear that very different behaviour occurs for Na₃Bi in Fig. M8(b). At low tunnelling current an exponential dependence with distance $I(z)$ is observed, but as the distance from tip and sample decreases the current saturates to a value around 1 nA, which occurs over a length scale of ~1 nm. This corresponds to the barrier height going to zero as the tip approaches the sample surface.

This effect results from a modification of Eqn. 6.1 due to the lowering of the potential barrier by the mirror potential seen by an electron in close proximity to a metal surface [40], and is most pronounced for low work-function materials, such as Na₃Bi. This is shown schematically in Fig. M8(c). As we show in detail below, the theoretical treatment indicates that the effect of the mirror potential at large distances is simply a rigid shift in distance of the region in which the exponential behaviour occurs. Thus, we can use the exponential region where Eqn. 6.1 is obeyed to determine the work function, and we can extrapolate Eqn. 6.1 to point contact to determine the tip-sample distance, provided a correction factor is applied to account for the rigid shift due to the mirror potential.

There has been significant work on modelling image potential effects and is well summarized in [41], whereby considering a simple model such as the square barrier depicted in Fig. M8(c) for long tip-sample distances, $\ln(2)/s \gg \Phi$ the tunnelling current can be expressed as

$$I_t = I_0 e^{-2z\sqrt{2\Phi}} e^{\ln(2)\sqrt{2\Phi}} \quad (6.3)$$

where the main effect of the image potential at very long tip-sample distances is to increase the tunnelling current by a constant factor $e^{\ln(2)\sqrt{2\Phi}}$. For $I_t = I_0$, we obtain the increased distance between tip and sample due to the image potential $s = \ln(2)/2\Phi$ in atomic units. Converting from atomic units to SI units gives s (Å) = $\left(\frac{\ln(2)}{2\Phi(\text{eV})}\right) * 1 \text{ Bohr} (\text{Å}) * 1 \text{ Hartree} (\text{eV}) = \left(\frac{\ln(2)}{2\Phi(\text{eV})}\right) * 0.529 \text{ Å} * 27.2 \text{ eV}$ such that eqn. 6.1 would underestimate z_0 by a distance of $5 \text{ Å}/[\Phi(\text{eV})]$.

This value however, is most likely an underestimation as shown in Fig. M8(d) (taken directly from Figure 10 of Ref. 41) where $\ln(I(s)/I_0)$ as a function of distance is plotted for the simple square barrier model described above (dashed line), and more sophisticated calculations incorporating DFT-LDA (full line) and a model developed by Pitarke et al., that accounts for both non-local and local exchange and correlation effects (dashed-dotted red line) [42]. At large s the models still show an exponential $I(s)$ with similar slope (Fig. M8(d)) but the distance at which similar current is achieved is increased by as much as a factor of 3 from the square barrier model, such that the underestimation of z_0 distance by Eqn. 6.1 is more likely to be $\sim 15 \text{ Å}/[\Phi(\text{eV})]$ [42].

To understand and quantify the tip-sample distance in Na₃Bi, we first extract the slope from the linear region in Fig. M8(b) (as shown by the black line). This fit yields a slope of 1.5 \AA^{-1} , and accounting for the bias of -300 mV yields a work function or barrier height of 2.3 eV. I vs z measurements (where z is the nominal distance between tip and sample as defined by the STM piezo controller with arbitrary zero) were taken at various negative and positive bias values and yielded work functions of $2.3 \pm 0.05 \text{ eV}$. This confirms a very low barrier height. From the above analysis we estimate that the effect of the mirror potential is to lead to an underestimation of z_0 in Eqn. 6.1 of $\sim 15 \text{ \AA}/2.3$ or $\sim 6.5 \text{ \AA}$.

In order to determine the exact value of z_0 , we assume that at $z_0 = 0$ (point contact) the conductance is on order the conductance quantum $e^2/h \approx 40 \text{ \mu S}$ which gives $I_0 = 12 \text{ \mu A}$ at a bias voltage of -300 mV. Then the fit to the exponential region of $I(z)$ in Fig. M8(b) to Eqn. 6.3 gives $z_0 = -13.2 \text{ \AA}$. This allows us to plot the absolute distance $s = z - z_0$ on the top axis of Fig. M8(b).

We are now in a position to estimate the tip-sample separation from the dI/dV measurements. For each dI/dV curve we extract a relative distance s for each dI/dV measurement by referencing the tunnelling current at -300 mV to the I vs. s data in Fig. M8(b).

The green and purple dI/dV spectra in Fig. 4(b) of the main manuscript have the following:

Green curve: At a bias of -300 mV has a tunnelling current of 26 pA. From the I vs z plot taken at -300 mV this corresponds to relative z distance of 1.3 \AA . Adding 13.2 \AA to account for point contact and mirror potential yields a tip-sample separation of 14.5 \AA .

Purple curve: At a bias of -300 mV has a tunnelling current of 570 pA. From the I vs z plot taken at -300 mV this corresponds to relative z distance of -3 \AA . Adding 13.2 \AA to account for point contact and mirror potential yields a tip-sample separation of 10.2 \AA .

We now have an estimate of the tip-sample separation, so to calculate a displacement field for each of our dI/dV measurements we need to calculate the potential difference i.e. the work function difference between the metallic tip and the few-layer Na₃Bi. The measured barrier height of 2.3 eV is an average of the tip and sample work functions, $\Phi_{Barrier} = (\Phi_{Tip} + \Phi_{Na_3Bi})/2$, meaning we need to know either the tip work function or measure the work function of the Na₃Bi.

The Kelvin probe technique was utilized to measure the work function of few-layer Na₃Bi. The work function was determined by measuring the contact potential difference of the Na₃Bi relative to a gold reference of known work function (determined by photoelectron spectroscopy secondary electron cutoff measurements). A work function for few-layer Na₃Bi of $1.7 \pm 0.05 \text{ eV}$ was measured using this technique. This value and the 2.3 eV potential barrier gives a tip work function of $2.9 \pm 0.05 \text{ eV}$, and a potential difference between tip and sample of $1.2 \pm 0.1 \text{ eV}$. It should be noted that this is significantly lower than the expected value for a PtIr tip, suggesting that Na atoms have been picked up by the tip and consequently lower the work function (work function of Na is 2.23 eV). Whilst Na atoms were picked up they have little influence on the tip density of states, as spectroscopy performed on Au(111) after measurements on Na₃Bi were completed revealed a flat LDOS near the Fermi energy.

Using the calculated potential difference and tip-sample separation from above allows us to calculate electric fields for dI/dV spectra on ML and BL Na₃Bi as shown in Fig. 4(b) for BL and Fig. M9 for ML, with the full data set of bandgap as a function of electric field shown in Fig. 4(c).

| | | | | | | |
|---------------|----------|--------------|---|---|---|--------------|
| E_z | C_{3v} | \checkmark | X | X | X | \checkmark |
| Na(2) vacancy | C_{3v} | \checkmark | X | X | X | \checkmark |

II. Na₃Bi Bilayer (BL)

For BL without Na(2) vacancy, the space group is $P\bar{3}m1$ (No. 164). The point group is D_{3d} . Both electric field and Na(2) vacancy break the inversion symmetry, and we summarize the details in Table 2. Figure M11 shows the Na₃Bi crystal structure for (d) pristine BL, (e) BL with Na surface vacancy and (f) BL with Na surface vacancy and electric field.

Table 2. Point group (PG) symmetry for BL Na₃Bi. The second and third rows indicate the effects of electric field (E_z) and Na(2) vacancy. Note: At zero electric field both pristine and Na(2) vacancy BL Na₃Bi are 2D quantum spin Hall insulators, with topological index $\nu \in \mathbb{Z}_2 = 1$.

| | | Crystalline Symmetries | | | | |
|---------------|----------|------------------------|--------------|--------------|--------------|--------------|
| | PG | C_{3z} | C_{2x} | I | S_{6z} | M_{yz} |
| pristine | D_{3d} | \checkmark | \checkmark | \checkmark | \checkmark | \checkmark |
| E_z | C_{3v} | \checkmark | X | X | X | \checkmark |
| Na(2) vacancy | C_{3v} | \checkmark | X | X | X | \checkmark |

From the above tables, one can observe that both BL/ML Na₃Bi possess the C_{3z} and C_{2x} rotational symmetries. The difference is that ML has mirror symmetry M_{xy} and BL has inversion symmetry I . In terms of symmetry breaking, the electric field does not break any additional symmetry that is not already broken by the Na(2) vacancy: For ML, both electric field and Na(2) vacancy break the horizontal mirror symmetry and C_{2x} rotation symmetry, and reduce the D_{3h} symmetry to C_{3v} symmetry; while for BL, they both break the inversion symmetry and C_{2x} rotation symmetry, and reduce the D_{3d} symmetry to C_{3v} symmetry. Hence, ML and BL share the same point group C_{3v} after symmetry breaking by electric field OR Na(2) vacancy.

However, for our discussion on the band topology, the crystalline symmetry is not relevant. This is because our main point is that in the absence of electric field, the ML/BL Na₃Bi (with or without Na vacancy) are quantum spin Hall insulators, which only require time reversal symmetry. Electric field does not break the time reversal symmetry, rather it drives a quantum spin Hall insulator $\nu \in \mathbb{Z}_2 = 1$ to trivial insulator $\nu \in \mathbb{Z}_2 = 0$ transition through a band ordering inversion due to the Stark effect.

Notes:

1. C_{nx} and C_{nz} are the rotations of $360^\circ/n$ with the rotation axis along x direction and z direction, respectively.
2. S_{nz} is the rotation of $360^\circ/n$ followed by reflection in a plane perpendicular to the rotation axis (along z direction).
3. M_{xy} , M_{xz} and M_{yz} are the mirror reflections with the mirror plane in the xy plane, xz plane and yz plane, respectively.

4. I is the inversion symmetry.

5. Symmetry relations: $S_{3z} = C_{3z}M_{xy}$; $M_{xz} = C_{2x}M_{xy}$; $S_{6z} = IC_{3z}$; $M_{yz} = IC_{2x}$.

Methods References

- [26] P. E. Blöchl, Projector augmented-wave method. *Physical Review B* 50, 17953 (1994).
- [27] J. P. Perdew, K. Burke, M. Ernzerhof, Generalized gradient approximation made simple, *Phys. Rev. Lett.* 77, 3865 (1996).
- [28] I. Souza, N. Marzari, D. Vanderbilt, Maximally localized Wannier functions for entangled energy bands. *Physical Review B*, 65, 035109 (2001).
- [29] M. L. Sancho, J. L. Sancho, Sancho, and J. Rubio, Highly convergent schemes for the calculation of bulk and surface Green functions. *Journal of Physics F: Metal Physics*, 15, 851 (1985).
- [30] Q. Wu, S. Zhang, H. F. Song, M. Troyer, and A. A. Soluyanov, WannierTools: An open-source software package for novel topological materials. *Computer Physics Communications* (2017).
- [31] A. D. Becke, E. R. Johnson, A simple effective potential for exchange, *J. Chem. Phys.* 124, 221101 (2006).
- [32] F. Tran, P. Blaha, Accurate band gaps of semiconductors and insulators with a semilocal exchange-correlation potential, *Phys. Rev. Lett.* 102, 226401 (2009).
- [33] D. Koller, F. Tran, P. Blaha, Improving the modified Becke-Johnson exchange potential, *Phys. Rev. B* 85, 155109 (2012).
- [34] M. T. Edmonds, J. Hellerstedt, K. M. O'Donnell, A. Tadich, M. S. Fuhrer, Molecular Doping the Topological Dirac Semimetal Na₃Bi across the Charge Neutrality Point with F4-TCNQ, *ACS Applied Materials and Interfaces*, 8, 16412 (2017)
- [35] A. Damascelli, Z. Hussain, Z.-X. Shen, Angle-resolved photoemission studies of the cuprate superconductors. *Rev. Mod. Phys.* 75, 474 (2003)
- [36] S. Hufner, *Photoelectron Spectroscopy: Principles and Applications* (Springer, Berlin 3rd Edition, 2003)
- [37] I. Battisti, V. Fedoseev, K. M. Bastiaans, A. De la Torre, R. S. Perry, F. Baumberger, and M. P. Allen, *Phys. Rev. B* 95, 235141 (2017)
- [38] R. Yu, X. L. Qi, A. Bernevig, Z. Fang, and X. Dai, Equivalent expression of Z_2 topological invariant for band insulators using the non-abelian Berry connection. *Physical Review B*, 84, 075119 (2011).
- [39] A. A. Soluyanov, D. Vanderbilt, Wannier representation of Z_2 topological insulators. *Physical Review B*, 83, 035108 (2011)
- [40] N. D. Lang, Apparent barrier height in scanning tunnelling microscopy, *Phys. Rev. B* 37, 10395 (1988)
- [41] J. M. Blanco, F. Flores, R. Perez, STM-theory: Image potential, chemistry and Surface relaxation, *Progress in Surface Science* 81, 403 (2006)
- [42] J. M. Pitarke, P. M. Echenique, F. Flores, Apparent barrier height for tunneling electrons in STM, *Surface Science* 217, 267 (1989)

Data Availability Statement

The data that support the findings of this study are available from the corresponding author upon reasonable request.

Extended Data Figure Legends

Figure M1. RHEED, LEED and XPS characterization of few-layer Na₃Bi. RHEED patterns of (a) Si(111) 7x7 reconstruction along $\bar{\Gamma} - \bar{M}$ direction and (b) few-layer Na₃Bi along the $\bar{\Gamma} - \bar{K}$ direction. (c) 1x1 LEED image of few-layer Na₃Bi taken at 32 eV. (d) XPS of Na 2p and Bi 5d core level taken at $h\nu$

= 100 eV for few-layer Na₃Bi. (e) Normalized XPS of Si 2p core level taken at 350 eV (left panel) and 850 eV (right panel). Each panel shows the Si 2p of the clean Si substrate (black curve) and with few-layer Na₃Bi grown on top. The spectra have been offset in intensity for clarity.

Figure M2. k_z band dispersion of few-layer Na₃Bi from photon-energy dependent ARPES measurements. Photon-energy dependent ARPES of ML/BL Na₃Bi demonstrating effectively 2D dispersion. Cut through the photon-energy ($h\nu = 45\text{-}55$ eV) dependent Fermi surface showing non-dispersion of the gapped Dirac valence band along k_z .

Figure M3. dI/dV spectra taken for mono- (red) and bilayer (black) Na₃Bi plotted on a (a) linear and (b) logarithmic scale. The logarithmic scale better accounts for the large change in intensity near the band edge. (c) Normalized dI/dV spectra at various tip-sample separations illustrating that the onset in intensity typically occurs at a normalized dI/dV signal of 0.01 within an error of ± 25 meV (when also accounting for tip-induced band bending). (d) Calculated tip-induced band bending, ϕ_{BB} using equation (3.1) for different biases.

Figure M4. (a) Two-dimensional Brillouin zone for Na₃Bi layered structures. Here we also show the projected 1D Brillouin zone used for studying the edge spectrum. (b-h) Results for monolayer (b-f) and bilayer (g-k) Na₃Bi with Na(2) vacancies [with one Na(2) vacancy in a 2x2 supercell]. (b,g) Electronic band structures, where the energy zero is set to be at the valence band maximum. (c, h) Orbitally resolved bandstructure without SOC and (d, i) orbitally resolved bandstructure with SOC. The red dots represent the contribution from the Na-s and Bi-s atomic orbitals, and the blue dots represent contribution from the Bi-p_x/p_y atomic orbitals. Band inversion induced by SOC can be clearly observed at Γ point for both ML and BL cases, which indicates that both ML and BL Na₃Bi are nontrivial 2D topological insulators. (e,j) Projected edge spectrum (edge along [010] direction), where pairs of \mathbb{Z}_2 topological edge states can be observed in the energy gaps (marked by the white arrows). (f,k) Calculated Wannier function center evolutions, which indicate a nontrivial \mathbb{Z}_2 invariant ($\mathbb{Z}_2 = 1$) for the bulk band structure in both monolayer and bilayer.

Figure M5. Extracting and fitting the dispersion relation from ARPES MDC and EDC spectra on few-layer Na₃Bi. (a) ARPES intensity plot along K- Γ -K direction after 30 minutes of K-dosing. (b) stack plots of MDCs for the valence band (left panel) and conduction band (right panel) extracted from (a). (c) EDCs extracted from (a). (d,e) Fitting extracted band coordinates by MDC and EDC analysis (red) to a hyperbola (d) and parabola (e), showing that Na₃Bi like bands are best described by a hyperbola function.

Figure M6. (a) Electron-band Fermi-surface of few-layer Na₃Bi after 30 minutes of K-dosing. (b) Radially averaged momentum profile through the Fermi surface, showing the ring structure at k_F . (c) Calculated charge-density assuming degeneracy of bands $g = 4$ using Eqn. (5.3) and the corresponding electric displacement field associated with the associated net charge transfer from the undosed film as a function of K-dosing time. Red points are as-measured, and green points are extrapolated based on the E_F shifting rate with K-dosing between 15-50 minutes.

Figure M7. Electric displacement field-dependence of topological insulator ML/BL Na₃Bi bands near E_F . (a) The sum of Δ parameters from the best fit of (3) to ARPES dispersion vs. applied electric displacement field. Both $\Delta_{n,p}$ are directly calculated from the high-field (purple) measurements, however at low-field (green) measurements, E_F is not sufficiently shifted for the electron dispersion to

be clearly resolved. Here we have used the ratio $\frac{\Delta_p + \Delta_n}{\Delta_p} \approx 1.4$ measured from the purple points to extrapolate Δ_n undoped film. (b) The valence edge (blue) and conduction edge (red) calculated from the fitted ARPES dispersion is shown for two high-symmetry directions: circles and squares as K - Γ - K and M - Γ - M respectively.

Figure M8. Tunnelling current as a function of relative tip-sample distance Z for (a) Au(111) (Bias +500 mV) and (b) thin film Na₃Bi (Bias -300 mV). The top axis in (b) represents the total distance, s , between tip and sample determined as described in Section M6. The black lines in (a) and (b) are exponential fits. (c) Energy-level schematic illustrating the effects of an image potential on the (purple trapezoidal) junction barrier; progression from blue, green, yellow, orange, and red curves indicate modification of the apparent barrier height due to the imaging potential at decreasing tip-sample distances s . (d) $\ln(I(s)/I_0)$ shown as a function of distance for a square barrier model (dashed line); DFT-LDA (full line); and image potential model (dashed-dotted red line). Data are taken from Figure 10 of Ref. 41.

Figure M9. Individual dI/dV spectra taken on ML Na₃Bi at different tip-sample separations (electric field). The spectra have been normalized and offset for clarity.

Figure M10. (a) Calculated bandgap variation as a function of electric field for monolayer Na₃Bi with Na(2) vacancy. The gap closes and reopens at ~ 1.85 V/Å. (b) 2D Brillouin zone and the projected 1D boundary Brillouin zone. (c-f) Orbital-resolved bandstructures and edge spectra for monolayer Na₃Bi at electric fields of 0.0 V/Å (c,d) and 2.5 V/Å (e,f), which are marked by points A and B in (a). (c) Orbital-resolved band structures with spin-orbital coupling (SOC) in the absence of electric field (the energy zero is set to be at the valence band maximum at Γ point). The red dots represent the contribution from the Na- s and Bi- s atomic orbitals, and the blue dots represent the contribution from the Bi- p_x/p_y atomic orbitals. A band inversion is observed at Γ induced by SOC, indicating that monolayer Na₃Bi is a nontrivial 2D topological insulator. (d) Projected edge spectrum (edge along [010] direction) in the absence of electric field, showing topological edge states. (e,f) are the corresponding results at electric field of 2.5 V/Å. In (e), the band ordering at Γ is inverted compared to (c), indicating a topological phase transition to a trivial insulator phase. This is confirmed by the disappearance of topological edge states as shown in (f).

Figure M11. Crystal structure and symmetries of monolayer and bi-layer Na₃Bi. (a) and (d) Pristine ML and BL Na₃Bi. (b) and (e) ML and BL with a Na surface vacancy. (c) and (f) ML and BL Na₃Bi with Na surface vacancy plus electric field applied perpendicular to the sample.

Main Figures

Figure 1.

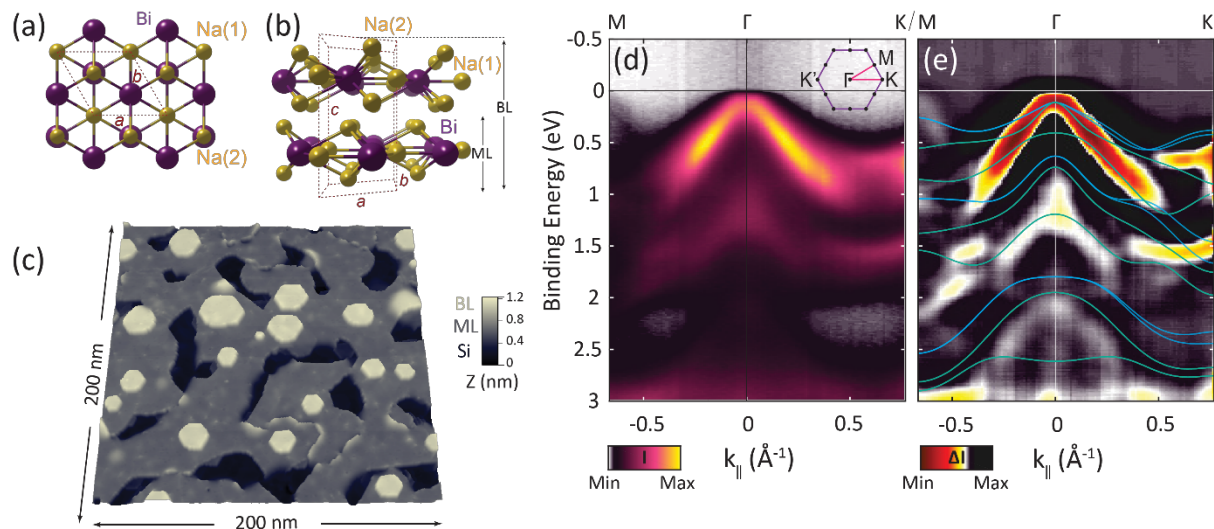


Figure 2.

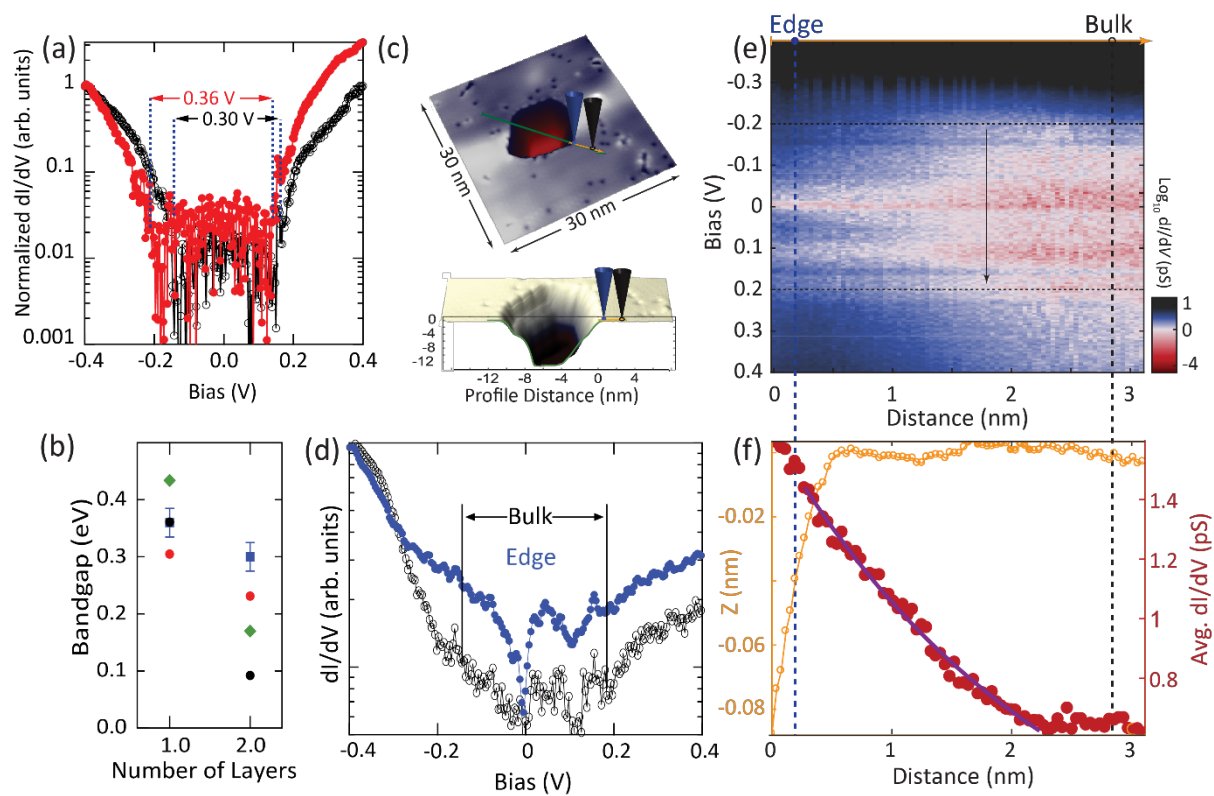


Figure 3.

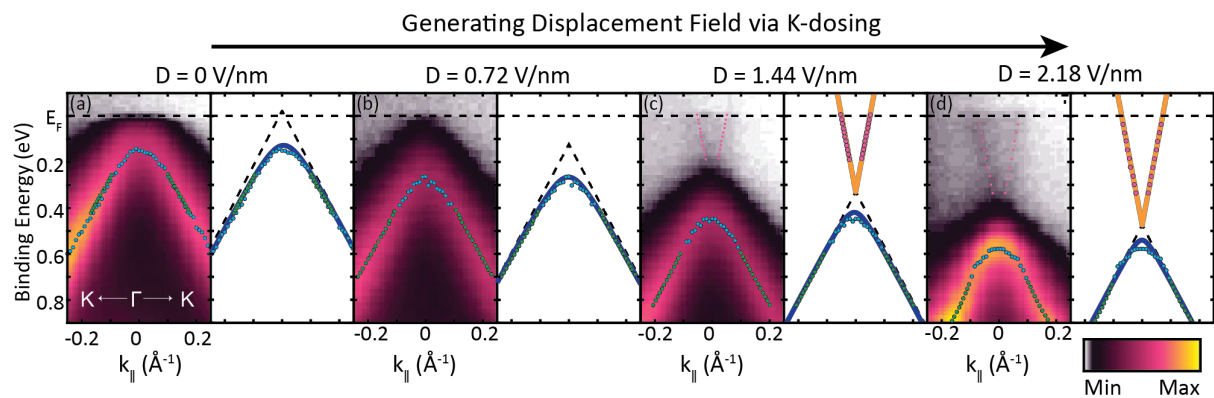
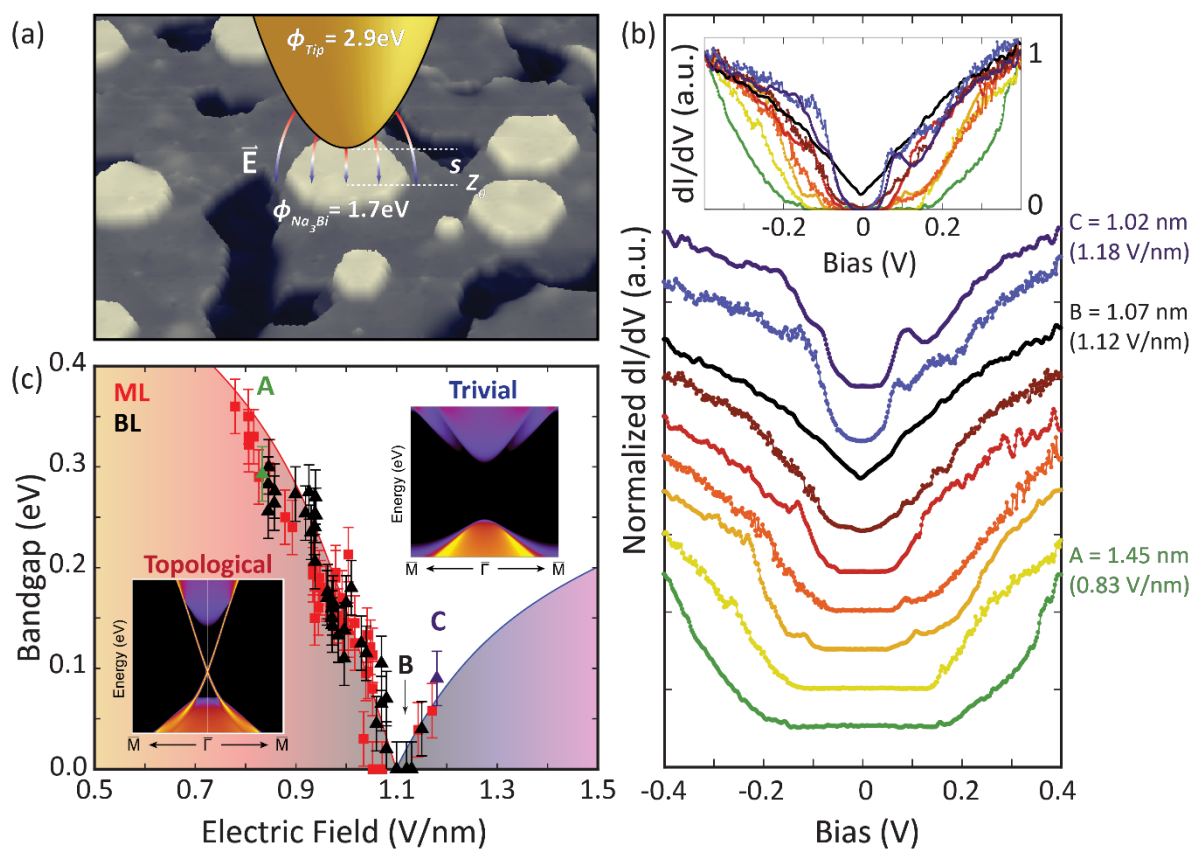


Figure 4.



Extended Data Figures

Figure M1.

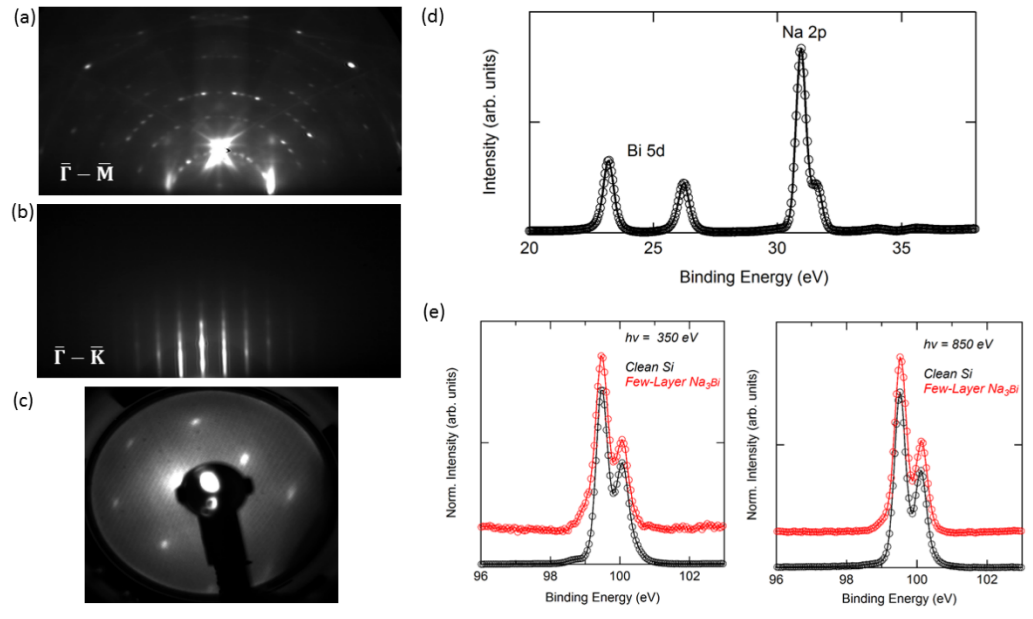


Figure M2.

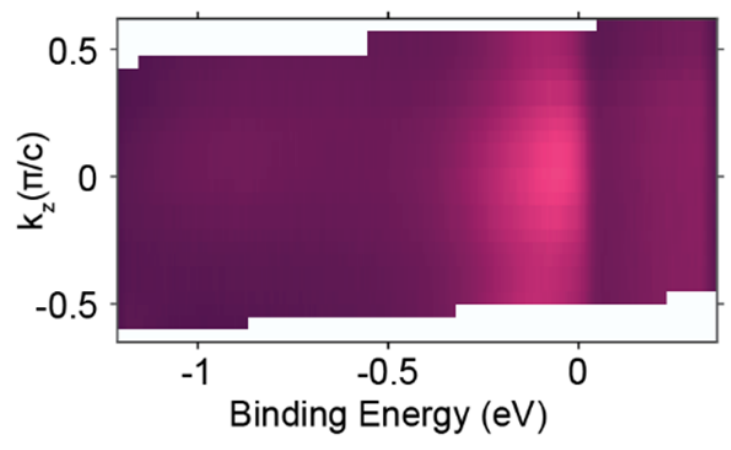


Figure M3.

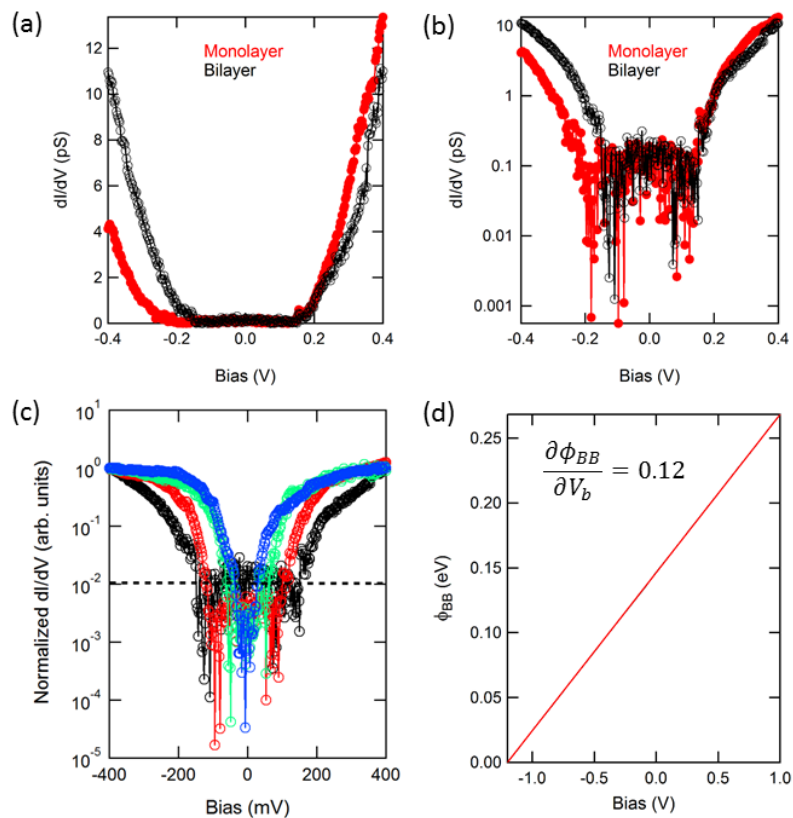


Figure M4.

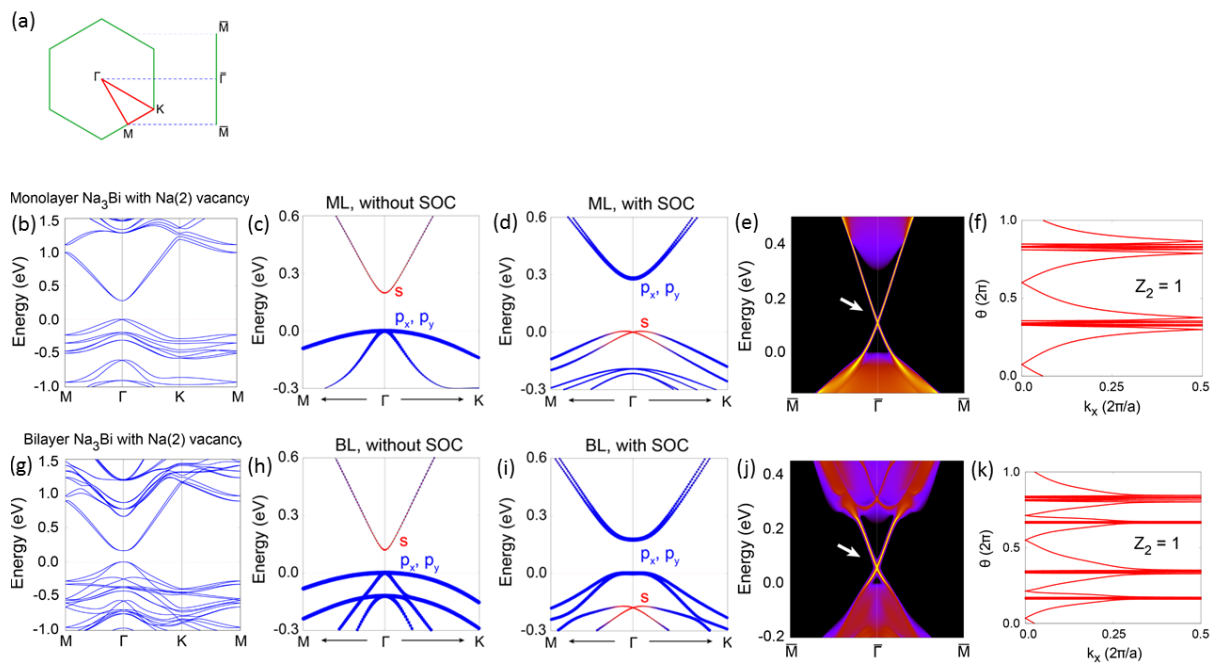


Figure M5.

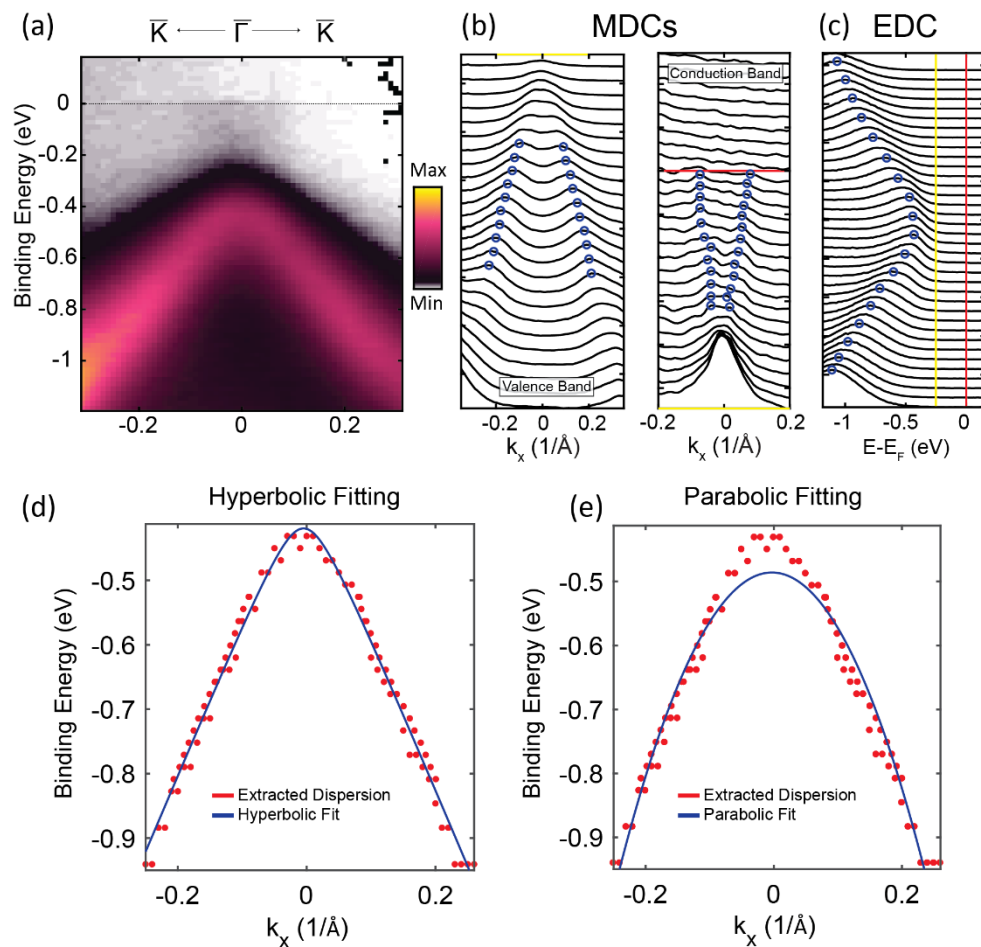


Figure M6.

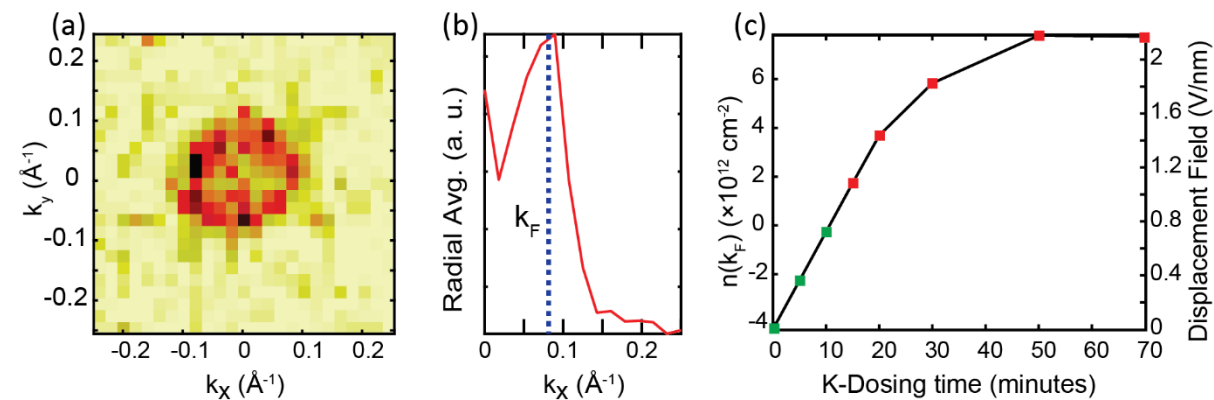


Figure M7.

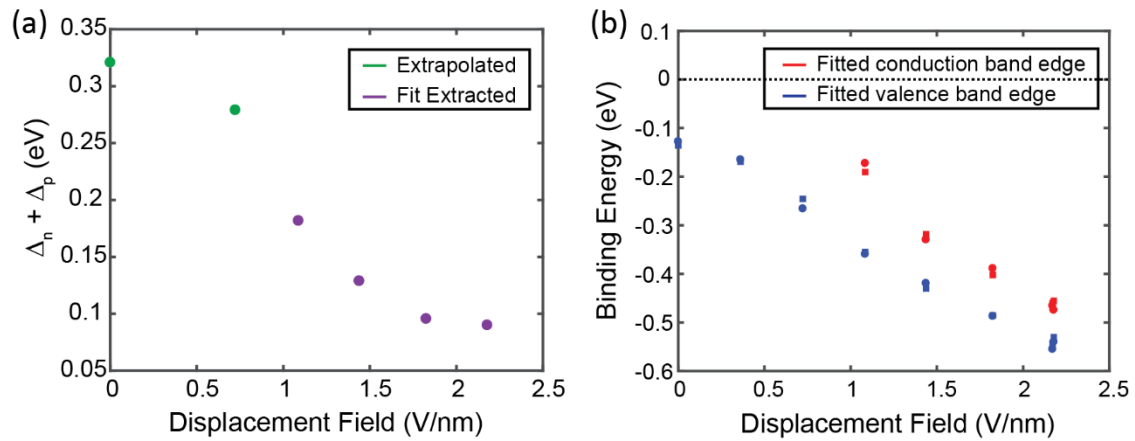


Figure M8.

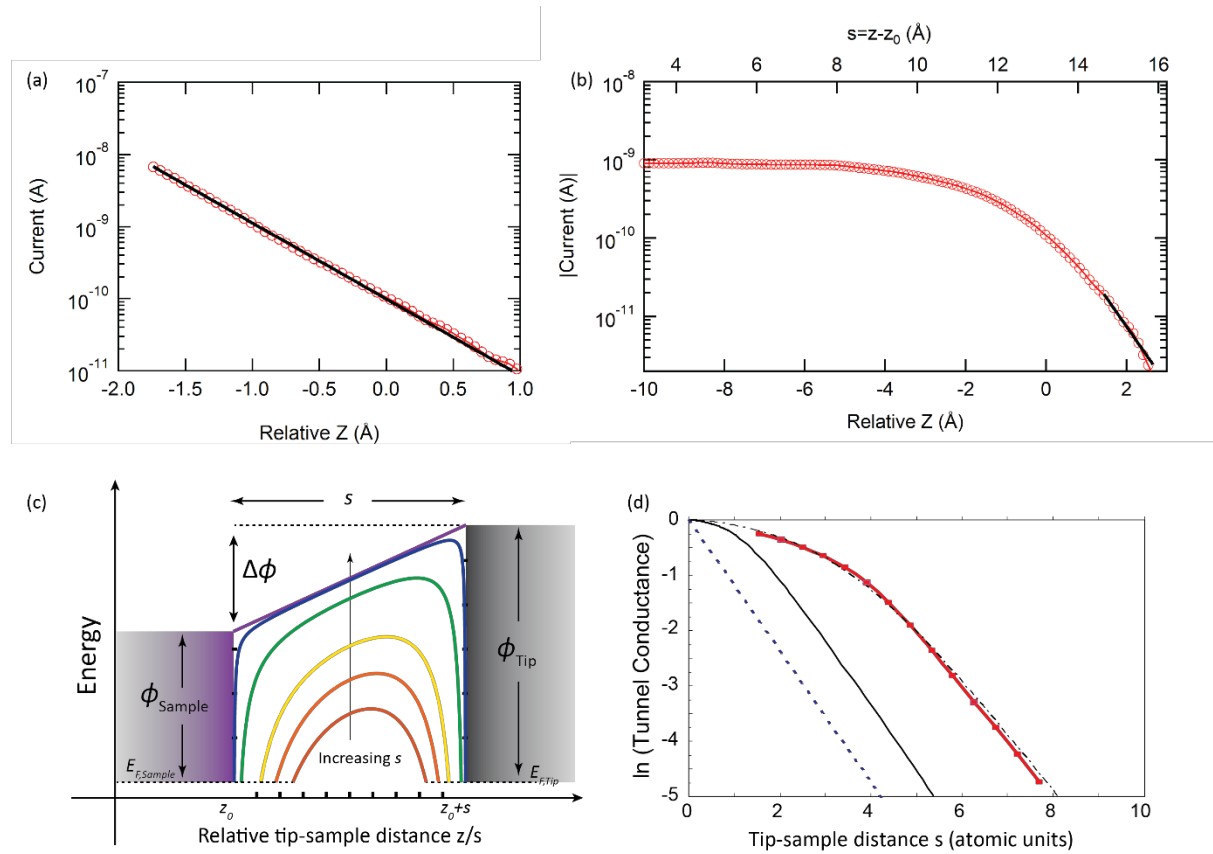


Figure M9.

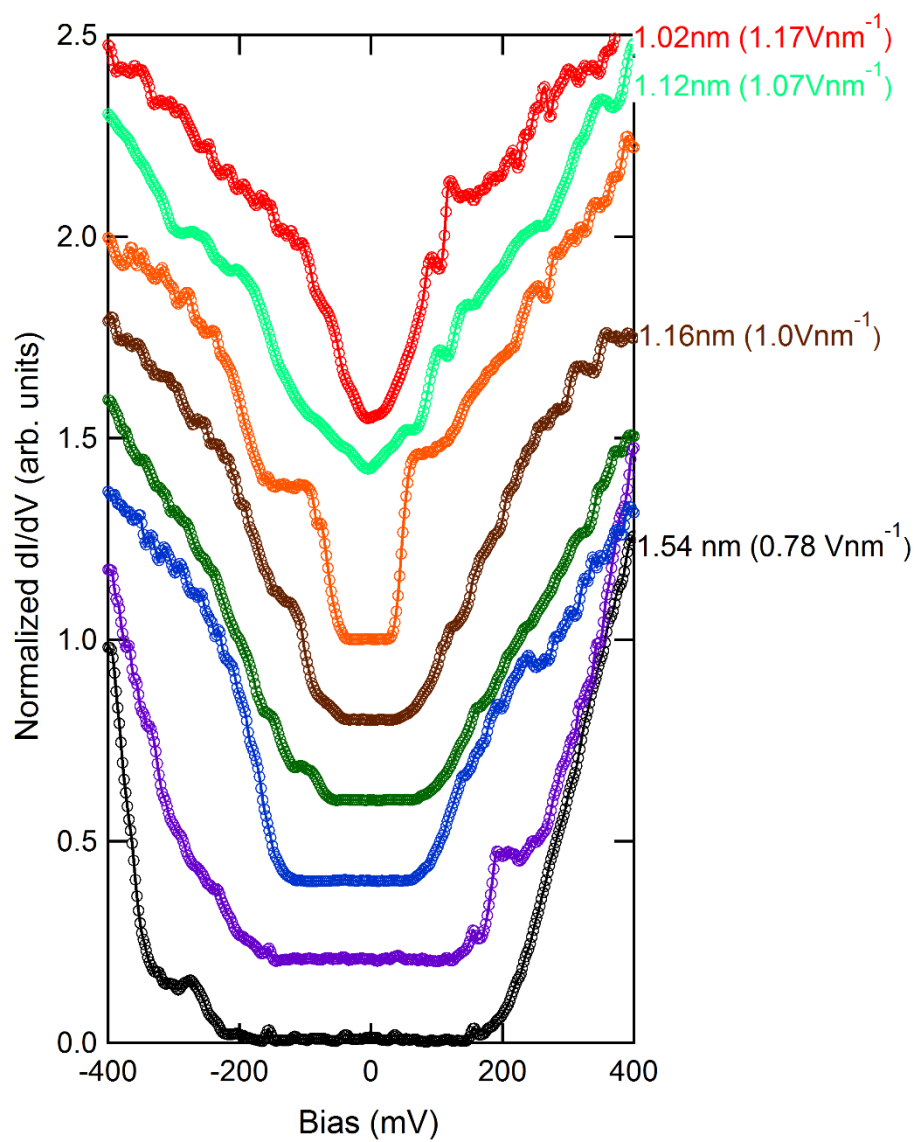


Figure M10.

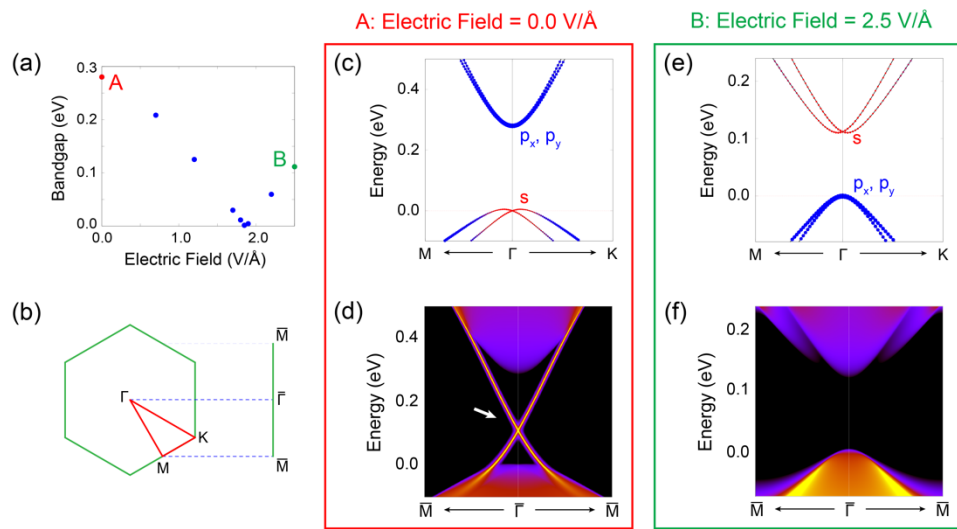


Figure M11.

